



A multiscale framework to predict electrochemical characteristics of yttrium doped Barium Zirconate based solid oxide cells

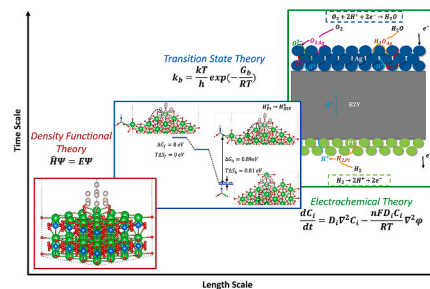
Pikee Priya, N.R. Aluru*

Department of Mechanical Science and Engineering, Beckman Institute for Advanced Science and Technology, University of Illinois at Urbana-Champaign, Urbana, IL, 61801, USA

HIGHLIGHTS

- A multiscale framework developed that could predict Current-Voltage characteristics.
- DFT, Transition State and Electrochemical Theory are coupled at different scales.
- Effect of temperature and environment on the characteristics is well manifested.
- Data-driven sensitivity analysis performed for low temperature SOC performance.

GRAPHICAL ABSTRACT



ARTICLE INFO

Keywords:

BZY
SOFC
SOEC
Current-Voltage
Reducing and oxidizing
Neural networks

ABSTRACT

A multiscale model is developed combining physics at atomistic, meso and continuum scales to predict the electrochemical characteristics of Current-Voltage curves in Yttrium doped Barium Zirconate based solid oxide cells. The most probable reaction pathway involving proton transfer from the surface of electrodes to the electrode/air/electrolyte Triple Phase Boundary from where it moves to the electrolyte is proposed, and their reaction barriers have been predicted from Density Functional Theory calculations. The model is validated against experimental observations. The environment, such as the amount of H₂ (reducing) and O₂ (oxidizing) gases the electrolyte is equilibrated in, affects the type of charge carriers while the temperature affects their rate of transport. Both these factors affect the rate of reactions in the proposed pathway. These effects are well manifested in the predicted electrochemical characteristics. The reducing environments are suitable for fuel cell mode operation and, the oxidizing environments are suitable for electrolyzer cell mode operations. The activation energy for conductivity in oxidizing environments is higher making it less amenable for low-temperature operation than in reducing environments. A data-driven sensitivity analysis is performed from which a non-intuitive parameter, permittivity of the electrolyte, is predicted to be important for Solid Oxide Cell performance.

1. Introduction

There is currently considerable effort to develop Solid Oxide Cells

(SOC) for low-temperature operation [1–10] to make energy conversion technology more usable and portable. A low-temperature operation can significantly reduce the cost of the materials required for interconnects

* Corresponding author.

E-mail address: aluru@illinois.edu (N.R. Aluru).

<https://doi.org/10.1016/j.jpowsour.2020.228969>

Received 21 December 2019; Received in revised form 30 July 2020; Accepted 16 September 2020

Available online 8 October 2020

0378-7753/© 2020 Elsevier B.V. All rights reserved.

in SOC stacks [11,12]. It can also reduce thermal stresses and material degradation which lead to shorter lifecycles. This is a common problem for high-temperature SOC materials [13–15]. Also, more research efforts are being put into energy storage technologies that can both generate power and produce fuel reversibly [16–19], along with resistance to degradation [20,21]. Proton conducting perovskites have proven to have high conductivities at intermediate temperatures because of low activation required for proton conduction and have also been used reversibly in the past [22–24]. Although, proton conduction dominates in reducing environments containing H_2 , electronic conduction of holes and transport of vacancies also contribute to electrochemical characteristics in oxidizing environments containing O_2 which are believed to have higher activation energy. This is a major impediment for low-temperature operation. Design of low temperature SOCs with enhanced proton conductivity relies on two determining factors: suitable material selection and establishing suitable operating conditions. In the current work, we discuss the behavior of a high proton conductivity material like Yttrium (15%) doped Barium Zirconate (BZY) under different operating conditions to setup design guidelines for suitability of a proton conductor for low temperature operations. This is made possible through a multiscale framework which integrates physics at all length (atomic to microstructure to cell) and time scales (atomic vibrational frequency to solid and gaseous diffusion time scales). This is accompanied by subsequent data-driven sensitivity analysis.

BZY is one of the best known proton conductors at intermediate temperatures [25–27]. Understanding its behavior is essential to design low temperature proton conducting material. In the current work, we explore proton conductivity for BZY based SOCs at different operating conditions through a multiscale framework which connects the physics at the atomistic, meso, and continuum scales. This singular framework is used to predict electrochemical characteristics in direct current conditions. We propose a reaction mechanism for proton transfer at the cathode/anode surface and air/electrode/BZY Triple Phase Boundary (TPB) interface, the reaction barriers for which, are calculated through atomistic Density Functional Theory (DFT) [28–30]. These reaction barriers are correlated to rate constants of reaction steps and diffusivities of species through the Transition State theory [31]. The various kinetic, thermodynamic and microstructural parameters are then used to solve for the transport of different charged species in a SOC in the continuum scale model.

Some of the initial modeling efforts in the early 2000's for SOFC stacks were mainly concentrated on temperature, flow or stress profile generated during operation [32–34]. The aim was to give an overall understanding of temperature/stress distributions in stacks rather than accounting for rigorous validation of electrochemical characteristics. It was later in the 2000's that the electrochemistry was taken into consideration, which could predict the characteristics and performance reasonably well [35–39]. However, the rate of reactions in the reaction pathways was based on fitted/empirical parameters which could not highlight the exact contribution of these reactions.

The effect of microstructure like porosity, tortuosity, specific surface area of the TPBs etc. have been considered recently in numerical models and have found to greatly affect the performance of SOCs [40–43]. Reconstruction of porous and bulk microstructures have also been done with applications in several fields [44–46]. However, a detailed validation of microstructural effects on SOFC characteristics has never been attempted. Numerical models that extract microstructural data from real microstructures are also scarce.

The current work overcomes the shortcomings as mentioned above, of the numerical models for SOCs that exist in literature to date. It takes kinetic parameters of rate constants and diffusivities from DFT calculations done in the present work or those performed in literature, rather than fitting them. Also, the microstructural features of the specific surface area of the porous electrodes and specific surface area of the TPBs at the electrolyte/electrode surface are estimated from real microstructures using stereological analysis, for the test case used for validation. A

parametric study of the microstructural features will be published elsewhere. The current work uses the framework to predict the Current Voltage characteristics.

The main objectives of the current study are:

- i. Develop a reliable multiscale model for predicting the Current-Voltage characteristics of BZY based SOFC/SOEC that could be extended to other solid oxides to minimize/augment experiments;
- ii. Study the effect of operating conditions such as temperature and environment, on these characteristics for optimum proton conductivity at low temperatures; and
- iii. Setup design guidelines in terms of material properties and operating conditions for low temperature proton conductivity through sensitivity analysis.

A unique multiscale framework that takes into consideration physics at nano, meso and continuum scales has been used to attain the above objectives.

2. Multiscale numerical model

2.1. Reaction pathway

The model SOC system consists of a porous 200 nm thick Pt anode layer, a 500 μm BZY electrolyte and a porous Ag layer, 500 nm in thickness as seen in Fig. 1. Electrochemical characteristics in BZY based SOCs is a result of the transport of charged carriers such as protons, oxygen vacancies and holes across the electrolyte. This transport across the electrolyte occurs along with a series of reactions at the anode surface, and subsequent reactions at the cathode surface. These proposed series of transport steps and reactions on the anode and cathode surfaces and in the electrolyte bulk are sequentially mentioned below and illustrated in Fig. 1:

(i) **Transport 1 (T1):** Diffusion of diatomic hydrogen gas molecules through the porous anode

(ii) **Reaction 1 (R1):** The hydrogen in the atmosphere at the anode side, adsorbs on the surface.



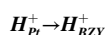
(iii) **Transport 2 (T2):** Diffusion of adsorbed hydrogen molecules on the anode surface

(iv) **Reaction 2 (R2):** The adsorbed hydrogen dissociates into protons at the anode surface

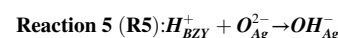


(v) **Transport 3 (T3):** The proton diffuses on the anode surface to reach the TPBs

(vi) **Reaction 3 (R3):** The proton transfers from the anode to the electrolyte at the TPB



(vii) **Transport 4 (T4):** Transport of protons across the electrolyte
(viii) The proton transfers from the electrolyte to the cathode at the TPB



- (ix) **Transport 5 (T5):** Diffusion of protons on the cathode surface
- (x) **Transport 6 (T6):** Diffusion of O_{Ag}^{2-} on cathode surface
- (xi) **Transport 7 (T7):** Diffusion of OH_{Ag}^- on cathode surface
- (xii) **Transport 8 (T8):** Diffusion of oxygen gas through the porous

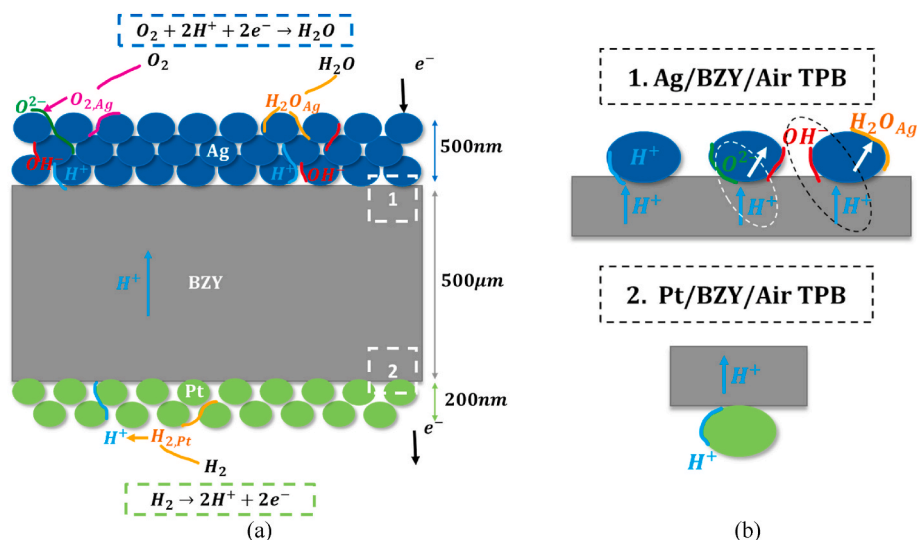


Fig. 1. (a) The SOC system showing the porous anode (Pt), electrolyte (BZY) and the porous cathode (Ag) with various surface reactions for transfer of protons from the anode to cathode in the fuel cell mode. The TPB areas are marked as 1 and 2 (b) The reactions at the cathodic Ag/BZY/air TPB (1) and anodic Pt/BZY/air TPB (2).

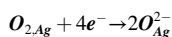
cathode

(xiii) **Reaction 7 (R7):** Oxygen gas adsorbs at the cathode surface

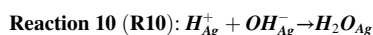
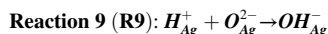


(xiv) **Transport 9 (T9):** Diffusion of adsorbed oxygen molecules on the cathode surface

(xv) **Reaction 8 (R8):** Adsorbed oxygen molecule dissociates on the cathode surface

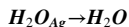


(xvi) Protons on the cathode surface react with other anions on the cathode surface



(xvii) **Transport 10 (T10):** Diffusion of adsorbed water molecules on the cathode surface

(xviii) **Reaction 11 (R11):** Water desorbs at the cathode surface



(xix) **Transport 11 (T11):** Diffusion of gaseous water molecules through the cathode pores.

2.2. Density Functional Theory

Vienna Ab initio simulation package (VASP) [29,47], version 5.3.5 was used to perform all spin-polarized DFT calculations with periodic boundary conditions. Generalized gradient approximation (GGA) exchange-correlation functional of Perdew-Burke-Ernzerhof (PBE) [48] was used. This method underestimates energy barriers by less than 10% for all the reactions at the TPB calculated using DFT + U method. A comparison of the energy barriers for the two techniques is provided in [Supplementary Material Section 4](#). The conjugate-gradient method was utilized to optimize the ionic positions until the Hellmann-Feynman forces on each ion were less than 0.04 eV/Å [49,50]. The energy convergence criterion was 10^{-5} eV. The plane-wave basis set cutoff energy was set to be 500 eV. The projector augmented wave (PAW) method [51] was used to calculate the interactions between valence electrons and nuclei plus core electrons. The PAW potentials with valence configurations of Ba ($5s^2 5p^6 6s^2$), Zr ($4s^2 4p^6 4d^2 5s^2$), Y ($4s^2 4p^6 4d^1 5s^2$), O ($2s^2 2p^4$), Ag ($4d^{10} 5s^1$), Pt ($5d^9 6s^1$) and H ($1s^1$) were

used.

The migration energy barriers and the transition state (TS) positions were calculated using the climbing image nudged elastic band method (CI-NEB) [52,53]. We used a $4 \times 4 \times 4$ Monkhorst-Pack [54] k-point mesh for bulk systems and used a $4 \times 4 \times 1$ Monkhorst-Pack k-point mesh for surface and interface systems. [Tables 1 and 2](#) provide the energy contributions from enthalpy and entropy as calculated through DFT in the current study or those adapted from literature for the reactions and transport steps, respectively.

The initial reaction pathway at the anodic side involves dissociative adsorption of H_2 on Pt which is well documented in the literature [55–60]. H_2 readily adsorbs on a Pt (111) (Reaction R1), the most stable surface, with an energy release. This energy is calculated to be 0.78 eV at an atop Pt site and 0.54 eV at a hollow fcc site by Olsen et al. [61], using the gradient-corrected functional of Perdew et al. [48]. However, at 600 °C, the activation barrier is reduced to 0.17 eV considering the entropy of molecular H_2 , which has much higher entropy than the adsorbed hydrogen molecule. The adsorbed H_2 molecule on the Pt surface moves freely on the Pt surface (Transport T2) with a very low migration barrier of 0.001 eV as calculated using DFT in our work. The desorption of protons from Pt (111) (Backward reaction R1) surface or clusters, on the other hand, is difficult as found using vibrational spectroscopy [62] and is calculated to be ~ 2.5 eV using DFT [63,64]. The migration barriers of protons on Pt (111) (Transport T3) and Ag(111) (Transport T5) surfaces are calculated to be 0.04 eV and 0.11 eV, respectively, in the DFT study of transition metal surfaces by Kristinsdóttir and Skúlason [65]. The vibrational frequencies of these reactions were calculated in this study using DFT.

The reactions at the cathodic surface involve dissociative adsorption of O_2 on the Ag surface, which has also been studied extensively using DFT [66–69] in the past. Presence of water molecules affects the barriers for O_2 adsorption and dissociation considerably. In the absence of water, there is an energy barrier of 0.19 eV for O_2 adsorption on Ag(111) (Reaction R7) surface which changes to a release of 0.57 eV in the presence of water [67]. This change was because of co-adsorption with H_2O molecules which lead to O–H hydrogen bonding, resulting in a more easily dissociating, activated O–O bond. The adsorbed oxygen prefers dissociation to oxide ions (Reaction R8) as found by the CI-NEB calculations. The barrier to dissociation reduces from 1.03 eV to 0.67 eV, as reported by Su et al. [70]. The reverse reaction, which is, the desorption barrier (Backward reaction R8), as reported by Wang et al. [71], is taken as 0.31 eV. The oxide ion on the surface migrates on the Ag (111) (Transport T6) surface with an energy barrier of 0.37 eV as

Table 1

The energy barriers calculated from DFT. References are provided for those taken from literature; other values have been calculated in this work. The colors represent reactions occurring at the Anode/Pt surface (Green), at the TPBs Pt/BZY/Air (R3), Ag/BZY/Air (R4-6) (Grey) and the Cathode/Ag surface (Blue). The reactions with ΔG of 0 eV for either the forward or backward reaction are the ones with no transition states. [61,64,70-73]

	Reaction Step	Forward Reaction (eV)			Backward Reaction (eV)		
		ΔE	$-T\Delta S$	ΔG	ΔE	$-T\Delta S$	ΔG
R1	$H_2 \rightarrow H_{2,Pt}$	-0.54	0.71	0.17	0.54[61]	0	0
R2	$H_{2,Pt} \rightarrow 2H_{Pt}^+ + 2e^-$	0	0	0	1.96[64]	-1.44	0.52
R3	$H_{Pt}^+ \rightarrow H_{BZY}^+$	0	0	0	0.87	0.02	0.89
R4	$H_{BZY}^+ \rightarrow H_{Ag}^+$	0.74	-0.26	0.48	1.43	-0.02	1.41
R5	$H_{BZY}^+ + O_{Ag}^{2-} \rightarrow OH_{Ag}^-$	0	0	0	1.81	0.04	1.85
R6	$H_{BZY}^+ + OH_{Ag}^- \rightarrow H_2O_{Ag}$	0.59	-0.07	0.52	0.56	-0.01	0.55
R7	$O_2 \rightarrow O_{2,Ag}$	0	0	0	0.57[70]	1.22	1.79
R8	$O_{2,Ag} + 4e^- \rightarrow 2O_{Ag}^{2-}$	0.67[70]	0	0.67	0.31[71]	-0.03	0.28
R9	$H_{Ag}^+ + O_{Ag}^{2-} \rightarrow OH_{Ag}^-$	0.12[72]	-0.01	0.11	2.38[72]	-0.04	2.34
R10	$H_{Ag}^+ + OH_{Ag}^- \rightarrow H_2O_{Ag}$	0.56[73]	0.07	0.63	0.5[73]	0.01	0.51
R11	$H_2O_{Ag} \rightarrow H_2O$	0.17[70]	0	0	-0.17	1.34	1.17

Table 2

The energy barriers calculated for migration steps from DFT. References are provided for those taken from literature. The colors represent transport occurring at the Anode/Pt surface (Green), in bulk BZY (Grey) electrolyte, and at the Cathode/Ag surface (Blue). The gaseous diffusion coefficients through porous electrodes are calculated from the Dusty Gas Model (Yellow). The *indicate the D_0 (diffusion constant) and E_a (activation energy) values needed for calculation of diffusion coefficients using the equation. $D = D_0 \exp(-E_a/RT)$. [65,71,74,75,78,83,84]

	Species	$\Delta E/D_{0*}$ (eV)/(m ² s ⁻¹)	$-T\Delta S$ (eV)	$\Delta G/E_{a*}$ (eV)	
T1	H_2	2.96×10^{-4} [83]	-	-	ANODE/Pt
T2	$H_{2,Pt}$	0.001	0.001	0.002	
T3	H_{Pt}^+	0.04[65]	0.02	0.06	
T4	H_{BZY}^+	2.47×10^{-7} *[78]	-	0.47*	ELECTROLYTE/BZY
T4	V_O^-	9.98×10^{-8} *[78]	-	0.86*	
T4	h^+	$\frac{1.1 \times 10^{-9}}{c_h} T^*$	-	1.56*	
T5	H_{Ag}^+	0.11[65]	-0.02	0.09	CATHODE/Ag
T6	O_{Ag}^{2-}	0.37[71]	-0.02	0.35	
T7	OH_{Ag}^-	0.13[84]	0.05	0.18	
T8	O_2	8.6×10^{-5} * [83]	-	-	
T9	$O_{2,Ag}$	0.31	-0.03	0.28	
T10	H_2O_{Ag}	0.07 [74,75]	0.07	0.14	
T11	H_2O	1.06×10^{-4} *[83]			

calculated by Wang et al. [71]. The migration of the oxide ion is relatively easier on Ag (110) with a barrier of 0.17 eV. However, the migration energy at (111) surface was used for calculations in this study for the sake of consistency. The vibrational frequencies at 0 K were calculated for all the reactions and diffusion steps, which were used to determine the temperature-dependent entropy contribution to the reaction barriers.

The formation of hydroxyl ions from protons and oxide ions on the Ag(111) surface (Reaction R9) is one of the cathodic surface reactions

considered in this work which has been studied by Montoya and Haynes [72] from first principles. Formation of hydroxyl is relatively easy with an energy barrier of 0.12 eV, whereas the reverse reaction is difficult with a steep energy barrier of 2.38 eV. The hydroxyl ions migrate (Transport T7) from one hcp site to the other, with an energy barrier of 0.13 eV. Water adsorption (backward reaction R11) is necessary when the SOC functions in electrolyzer mode. Water molecules readily adsorb on Ag (111) surface releasing 0.17 eV [70] of energy. The dissociation of water on Ag(111) (Reaction R10), which is the next important step, has

also been systematically studied using DFT by Wang et al. [73]. This work reported a considerable difference in dissociation barriers which changes from 1.95 eV to 0.5 eV in the presence of pre-adsorbed oxide ions on the Ag surface, which is true on the cathodic side of the SOC in the present study. The migration of adsorbed H₂O molecule on Ag (111) surface (Transport T10) has been adopted from the works by Michaelides [74] and Ranea et al. [75]. Michaelides calculated the energy barrier for adsorbed H₂O molecules on (111) Ag surface through NEB and found it to be the difference of adsorption energies on the atop and bridge sites which is 0.07 eV [74]. The calculated entropy terms for all the reactions not involving gaseous reactants or products were found to be low (~0.02–0.05 eV).

The moving species for the SOC are either in the gaseous state moving through the porous electrodes, adsorbed gaseous molecules or dissociated ions on the surface of the electrodes. The translational, rotational, vibrational and PV-work contributions of the gaseous molecules are added to the energy barriers at 0 K [76]. Diffusivities for the gaseous species have been calculated using the ‘Dusty Gas Model’ which takes care of the molecular as well as Knudsen diffusion [77]. The diffusivities of the proton and oxygen vacancies in the BZY have already been reported from experiments and has been taken from the literature [78]. The diffusivity of holes in BZY is calculated from hole conductivities at different temperatures by Kuz'min et al. [79] and the relationship of diffusivity with conductivity for protons is provided by equation (1) in the work of Yamazaki et al. [80]. The activation energy for holes varies with temperature and concentration of holes.

The reaction barriers at the TPB (Pt/BZY/air and Ag/BZY/Air) involving direct transfer of protons or reaction of protons with other species were calculated in this study using CI-NEB DFT calculations. The effect of defects of acceptor dopants on the reactions has not been considered. A charge-neutral triple boundary configuration with a tetrahedral ((001) at the interface) fcc cluster of 10 Pt/Ag atoms on top of a (001) Ba-terminating BZY 5-layered crystal was structurally optimized for the calculations. The cluster size is chosen to keep the

contacting area for the porous electrode and TPB less than 10% (8.3%) which is typically true in experiments, so, the effect of the size of the cluster has not been considered. The cluster is a tetrahedra to keep the low surface energy surfaces (111) in contact with the (001) BZ and the air which is what has been seen by Shishkin and Ziegler [81]. The optimized structures are shown in the [Supplementary Material Section 1](#). The metal atoms attach to the O atoms in the BZY surface, making an angle of 79–83°. While Pt lattice parameter for the optimized structure is found to be 3.925 Å as compared to 3.924 Å for pure Pt, the Ag lattice parameter is found to be 4.159 Å as compared to 4.085 Å for pure Ag. We chose a Ba terminated structure as it is more favorable than having Zr/Y on the surface, as reported by Malagoli et al. [82].

The initial, transition and final configurations for reactions R3 at the Pt/BZY/air and R4, R5 and R6 at the Ag/BZY/air are shown in [Fig. 2](#). While proton readily transfers to BZY at the TPB configuration with an energy release of 0.87 eV, proton transfer from BZY to Ag has an energy barrier of 0.74 eV. Protons moving from Ag to BZY is an even more uphill process needing activation energy of 1.43 eV as shown in [Fig. 2](#)(a) and (b). The proton on the BZY surface readily reacts with an oxide ion on the Ag at the TPB with an energy release of 1.85 eV as shown in [Fig. 2](#)(c) and is the most energetically favorable pathway for protons in the SOFC mode. An alternate route of transfer of protons is through reaction with the OH⁻ ion at the TPB to form an adsorbed water molecule. This reaction has an activation barrier of 0.59 eV at 0 K which seems to be the most energetically favorable pathway in the SOEC mode when the proton transfers from Ag to BZY. The detailed enthalpy and entropy contributions for various reaction and transport steps at 600 K are provided in [Tables 1 and 2](#), respectively. [Fig. 3](#) provides a comprehensive energy landscape for all the reactions considered in this work.

2.3. Transition State Theory

The energy barriers for various reaction steps calculated through DFT are used to calculate the rate constants for all the 11 reaction steps

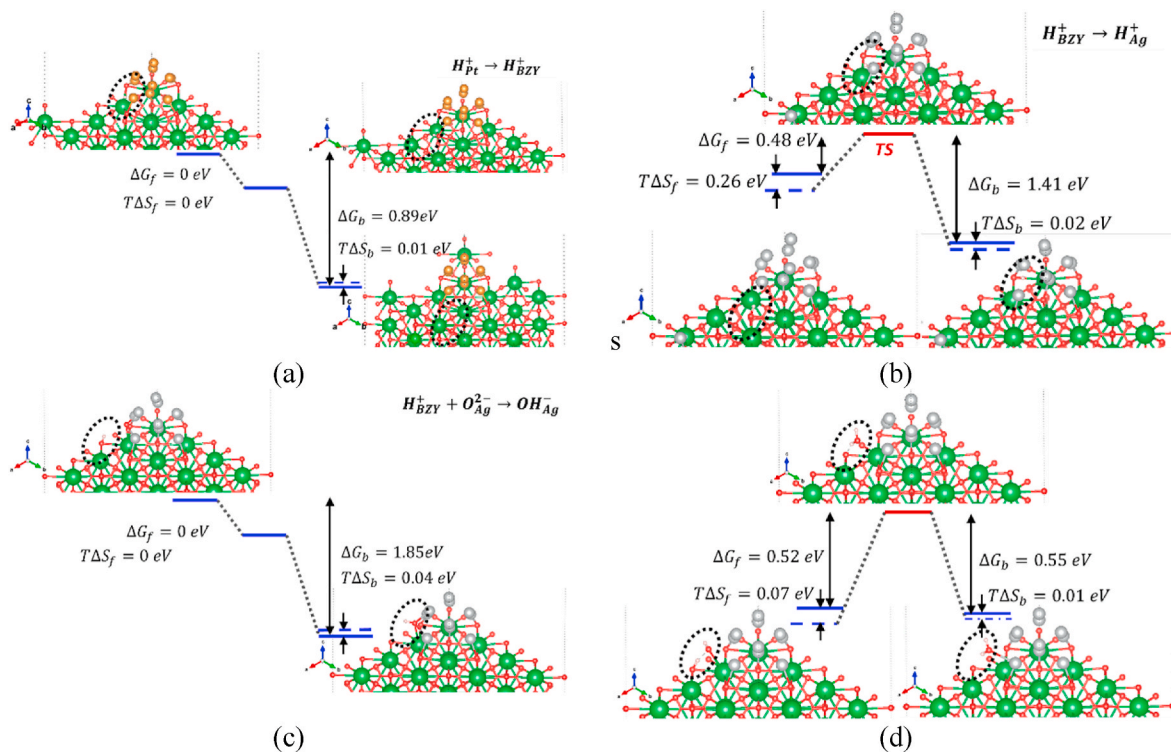


Fig. 2. The energy landscape at 600 °C for the reactions at the Pt/BZY/air TPB (a) R3 and at the Ag/BZY/air TPB (b) R4, (c) R5, (d) R6. Ba: Green, O: Red, Pt: Gold, Ag: Silver, H: White. The calculated entropy contributions ($T\Delta S$) to ΔG for all the reactions are also shown. (For interpretation of the references to color in this figure legend, the reader is referred to the Web version of this article.)

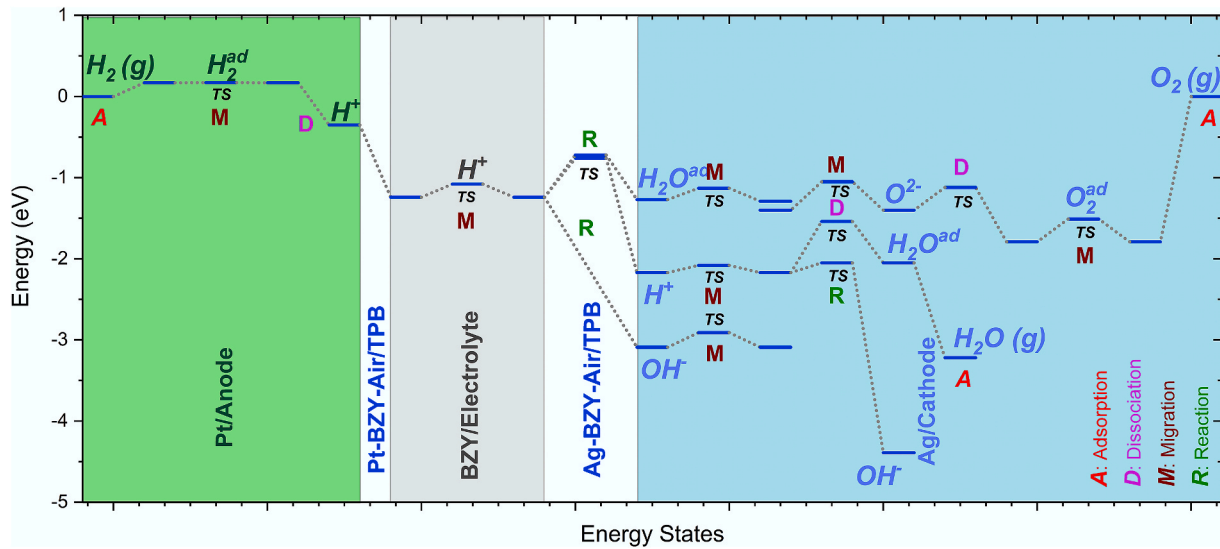


Fig. 3. The energy landscape of all the Reaction (R) (including Adsorption (A) and Dissociation (D)) and Transport (M/Migration) steps. The species and reactions on different surfaces are color coded, Pt/Anode (green), BZY/Electrolyte (grey) and Ag/Cathode (blue). (For interpretation of the references to color in this figure legend, the reader is referred to the Web version of this article.)

(R1-R11) using Eqn. (1). The diffusivities of adsorbed molecules (T2, T9 and T10) and charged ions (T3, T5, T6 and T7) on the surface of the cathode and anode are calculated using Eqn. (2). Equations (1) and (2) are derived using the Transition State Theory [31,85] for thermally activated processes. This theory assumes quasi-equilibrium between reactants and activated complexes in the transition state. The Eyring formulations [86] relating reaction rate constants, k , and diffusivities, D to free energy barriers obtained from DFT calculations are:

$$k = \frac{k_B T}{h} \exp\left(-\frac{\Delta G(T)}{k_B T}\right) \quad (1)$$

$$D = \frac{\lambda^2}{z} \frac{k_B T}{h} \exp\left(-\frac{\Delta G(T)}{k_B T}\right) \quad (2)$$

where k is the reaction rate constant, D is the diffusivity; k_B denotes the Boltzmann constant, T is the temperature, h denotes the Planck's constant, λ is the mean free path, z is the degrees of freedom and ΔG is the calculated Gibbs free energy.

2.4. Continuum Scale Modeling

The continuum scale model for the SOC consisting of the anode, electrolyte and cathode is setup in OpenFOAM [87,88]. The model solves for the transport of all the species involved using the Nernst-Planck equation (Eqn. (3)), under the influence of concentration and potential gradients, with reaction rates at the interfaces acting as source terms for the species. The distribution for electric potential based on charge distribution is given by the Poisson's Equation (Eqn. (4)),

$$\frac{dC_i}{dt} = D_i \nabla^2 C_i - \frac{nFD_i C_i}{RT} \nabla^2 \phi + S_i \quad (3)$$

$$\nabla^2 \phi = \frac{\rho}{\epsilon_0 \epsilon_r} \quad (4)$$

where, C_i and D_i are the concentration and diffusion coefficient of the species i , F is the Faraday's constant, R is the gas constant, ϕ is the electric potential, n is the number of charges involved in the reaction, T is the temperature, S_i is the source term due to reactions at the free surface and the interfaces, ρ is the charge density and ϵ_0 is the permittivity of vacuum, and ϵ_r , the relative permittivity. A detailed description of the transport equations for the different species is provided in Section

2 of the Supplementary Material.

The current at the anode, I_A is caused due to transfer of protons from anode to electrolyte at the TPB through reaction R3 and that at the cathode, I_C is due to transfer of protons from electrolyte to cathode due to reactions R4, R5 and R6 expressed as:

$$I_A = F r_3 \quad (5)$$

$$I_C = F(r_4 + r_5 + r_6) \quad (6)$$

where r_i is the rate of reaction $R(i)$. The rates of reactions R1 to R11 are calculated through the following expressions for a generalized reaction:

$$A \rightarrow B \quad (7)$$

If A and B are charged species and the reaction involves a charge transfer then,

$$r_i = A_S \left\{ k_i^+ \exp\left(\frac{-\alpha_j F \eta_j}{RT}\right) C_A - k_i^- \exp\left(\frac{(1-\alpha_j) F \eta_j}{RT}\right) C_B \right\} \quad (8)$$

where, A_S is the specific surface area, S can be Pt free surface, Ag free surface or the Pt/BZY/air TPB or Ag/BZY/air TPB; k_i^+ and k_i^- are the rate constants for forward and backward reactions, α_j is the charge transfer coefficient and η_j is the overpotential for electrode j . C_A and C_B are the concentrations of the reactants and the products respectively. Similarly, for no charge transfer, the reaction rates are:

$$r_i = A_S \{ k_i^+ C_A - k_i^- C_B \} \quad (9)$$

A detailed description of the rate constants for R1 to R11 are provided in the Supplementary Material Section 3.

The boundary conditions for the anode, electrolyte and cathode multilayer system are provided in Table 3:

Table 4 shows the values of the microstructural parameters of porosity and tortuosity and specific surface and TPB areas considered in the study.

The surface area per unit volume, S_V is estimated from real microstructures of the porous Pt and Ag electrodes is provided in the experimental validation test case from Iguchi et al. [89] using stereology as: $S_V = 2P_L$ where, P_L is the average number of points on the 2D surface per unit length. The specific TPB length per unit area, L_A is calculated using: $L_A = (\pi/2)P_L$ [90].

Table 3
Boundary conditions at different boundary patches.

Bottom of Anode layer:	Top of Cathode layer:
$\nabla C_i = 0, i = H_{Pt}^+, H_{2,Pt}, e^-$	$\nabla C_i = 0, i = H_{Ag}^+, O_{2,Ag}, O_{Ag}^{2-}, OH_{Ag}^-, H_{2O,Ag}, e^-$
$C_{H_2} = \text{constant}$	$C_{O_2} = \text{constant}, C_{H_2O} = \text{constant}$
$\phi = V_A$	$\phi = V_C$
Pt/BZY/air TPB:	Ag/BZY/air TPB:
$\nabla C_i = 0, i = H_2, H_{2,Pt}, e^-$	$\nabla C_i = 0, i = O_{2,Ag}, H_2O, H_2O, O_2, e^-$
$-\frac{\epsilon_{Pt}}{\tau_{Pt}} D_{H_{Pt}^+} \left(\nabla C_{H_{Pt}^+} + \frac{FC_{H_{Pt}^+}}{RT} \nabla \phi \right) = -r_3$	$-\frac{\epsilon_{Ag}}{\tau_{Ag}} D_{H_{Ag}^+} \left(\nabla C_{H_{Ag}^+} + \frac{FC_{H_{Ag}^+}}{RT} \nabla \phi \right) = r_4$
$-D_{H_{BZY}^+} \left(\nabla C_{H_{BZY}^+} + \frac{FC_{H_{BZY}^+}}{RT} \nabla \phi \right) = r_3$	$-D_{H_{BZY}^+} \left(\nabla C_{H_{BZY}^+} + \frac{FC_{H_{BZY}^+}}{RT} \nabla \phi \right) = -r_4 - r_5 - r_6$
	$-\frac{\epsilon_{Ag}}{\tau_{Ag}} D_{O_{Ag}^{2-}} \left(\nabla C_{O_{Ag}^{2-}} + \frac{FC_{O_{Ag}^{2-}}}{RT} \nabla \phi \right) = -r_5$
	$-\frac{\epsilon_{Ag}}{\tau_{Ag}} D_{OH_{Ag}^-} \left(\nabla C_{OH_{Ag}^-} + \frac{FC_{OH_{Ag}^-}}{RT} \nabla \phi \right) = -r_6$

Table 4
Value of the parameters used in the continuum model.

Parameter	Anode-Pt		Cathode-Ag	
Specific Surface Area	$A_{Pt} \text{ (m}^{-1}\text{)}$	5.21	$A_{Ag} \text{ (m}^{-1}\text{)}$	7.18
Specific TPB surface Area	$A_{Pt-TPB} \text{ (mm}^{-1}\text{)}$	4.16	$A_{Ag-TPB} \text{ (mm}^{-1}\text{)}$	5.64
Porosity	ϵ_{Pt}	0.5	ϵ_{Ag}	0.5
Tortuosity	τ_{Pt}	1	τ_{Ag}	1

3. Validation

The multiscale model was validated against experimental results provided in the literature. Fig. 4 shows the comparison of the Current-Voltage (IV) characteristics predicted by the multiscale model with that of the fuel cell operation of a BZY based solid oxide cell with Pt anode and Ag cathode from experiments performed by Iguchi et al. [89]. The thickness of the different components and the partial pressures of gases are kept like those in the experiments. A reasonable match between the numerical and experimental IV-curve at 600 °C, with a coefficient of correlation of 0.993 is seen. The IV-characteristics have been used for further analysis.

The Area Specific Conductivity (ASC) of the Pt anodes, Ag cathodes and BZ15Y from the simulations at 600 °C and 650 °C are within the range of the experimental work by Iguchi et al. [89]. The ASC found at

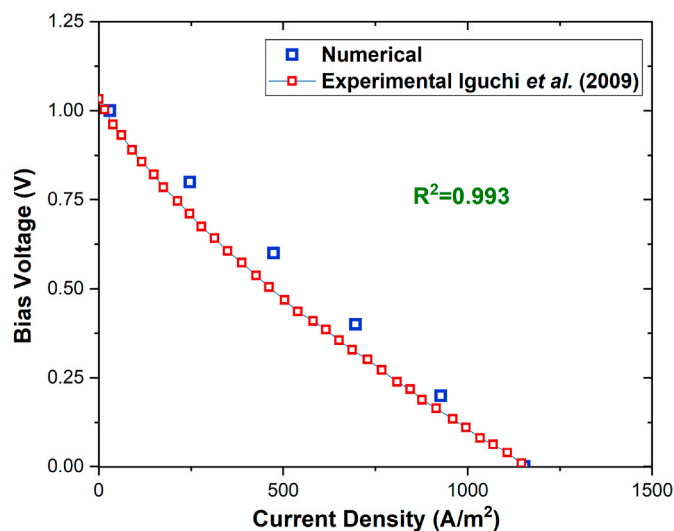


Fig. 4. Comparison of the IV Characteristics and for BZY with experiments performed by Iguchi et al. [89] showing reasonable accuracy.

600 °C–650 °C for the Pt anode and BZ15Y electrolyte at 600 °C are 1.02 S/cm² and 0.35 S/cm² compared to experimental values of 1.27 S/cm² and 0.2 S/cm² respectively. These decrease to 0.74 S/cm² and 0.24 S/cm² respectively at 650 °C validating the prediction of the effect of temperature on ASC.

4. Results and discussion

The operating conditions, such as temperature and environment, can have a profound effect on SOC performance. While the environment affects the type and concentration of charge carriers, the temperature affects the rate of transport. Both the above factors affect the reaction rates at the electrode surfaces and TPBs. In a SOC, the electrolyte can either be equilibrated in the gaseous atmosphere on the anodic side, which is humid (7.3% H₂O) hydrogen or in the atmosphere in the cathodic side, which is wet (3% H₂O) oxygen. In this work, the first case is referred to as a reducing atmosphere case, while the latter case is referred to as the oxidizing atmosphere case.

4.1. Effect of environment

Protons, vacancies and holes are the major charge carriers in proton-conducting solid oxide electrolyte like BZY. The concentrations are determined by the equilibrium hydration reaction: $H_2O + V_o^\bullet + O_o^\bullet \rightarrow 2OH_o$ in Kroger-Vink notation. The equilibrium constants K_{OH} for the reactions at different temperatures are taken from the work of Kreuer et al. [78,91] and can be expressed as:

$$K_{OH} = \frac{[OH_o]^2}{[V_o^\bullet][O_o^\bullet] \left(\frac{p(H_2O)}{p^0(H_2O)} \right)} \tag{10}$$

$K_{OH} = e^{(-\Delta H + T\Delta S)/RT}$ where ΔH and ΔS are the enthalpy and entropy of hydration for BZY.

Also, for charge neutrality

$$2[V_o^\bullet] + [OH_o] + [h] = [Y_{Zr}'] \tag{11}$$

To maintain the stoichiometry

$$[O_o^\bullet] + [V_o^\bullet] + [OH_o] = 3 \tag{12}$$

However, in oxidizing atmospheres, the formation of holes is accentuated by high O₂ activities through the reaction: $1/2O_2 + V_o^\bullet \rightarrow O_o^\bullet + 2h$. The equilibrium constant for this reaction is given by

$$K_h = \frac{[h]^2 [O_o^\bullet]}{[V_o^\bullet] \left(\frac{p(O_2)}{p^0(O_2)} \right)^{1/2}} \tag{13}$$

where $K_h = e^{-\ln \left(\frac{p(O_2)}{p^0(O_2)} \right) / 2}$ from work by Tsvetkov et al. [92]. Eqns (10-13) are simultaneously solved to give the concentrations of the charge carriers in BZY in both reducing and oxidizing atmospheres which the BZY is equilibrated in. It mainly effects the initial concentration of the charge carriers when solving for the Nernst Planck Equation (3).

The effect of partial pressures of H₂ at the hydrogen-electrode side and O₂ at the oxygen electrode sides in reducing condition, when the BZY electrolyte is equilibrated in the H₂ atmosphere is studied. Similarly, the effect of H₂ and O₂ partial pressures, in an oxidizing condition, when the electrolyte is equilibrated in the O₂ atmosphere, is studied. An operating voltage of 0 V is chosen for fuel cell operation and 2 V is chosen for the electrolysis cell operation. The partial pressure of H₂ is varied between 0.01 atm and 1 atm, whereas the O₂ partial pressures are varied between 0.02 atm and 2 atm.

The effects of partial pressures on the anode and cathode sides

equilibrating the electrolyte in the Pt side (reducing) or Ag side (oxidizing) atmospheres on the current density and proton conductivity is shown in Fig. 5. With an increase in H₂ pressure at the Pt electrode side, we see an increase in current density in SOFC mode (1929 A/m² at 0.01atm to 2120.6 A/m² at 1 atm H₂) and a decrease in the current in the SOEC mode (898.3 A/m² at 0.01atm to 215.2 A/m² at 1 atm H₂). The current density in both modes is higher if the electrolyte is equilibrated in the H₂ atmosphere (reducing) than if the electrolyte is equilibrated in the O₂ containing atmosphere (oxidizing). It should be noted that the H₂O content is kept constant at 0.073 atm at the Pt side and 0.023 atm at the Ag side which essentially means the effect of water on the number of protons is the same in all reducing atmosphere cases and oxidizing atmosphere cases. Oxidizing atmosphere cases are equilibrated in 0.2 atm O₂ with the water (0.023 atm) content which leads to lower proton content due to formation of holes. The proton conductivity seems to remain unaffected by the H₂ partial pressure on the Pt side when the electrolyte is equilibrated in the oxidizing environment. However, the Open Circuit Voltage (OCV) increases from 0.96 V at 0.01 atm (comparable to experimentally observed 0.953 V at 0.02 atm H₂ by Sun. et al. [93]) to 1.1 V at 1 atm H₂. The same is true for proton conductivity in the reducing atmosphere case in SOFC mode. However, having very high H₂ (1 atm) partial pressure on the Pt side in SOEC mode decreases the proton conductivity as higher H₂ leads to a higher rate of proton transfer at the TPB, than diffusion away from it, into the electrolyte causing higher charges and electric potential on the Pt/BZY interface. This

potential build-up on the anodic side decreases the overall electromotive force (emf) of the cell.

Similar trends are seen for the effect of O₂ partial pressure on the currents in SOFC and SOEC modes, as seen in Fig. 5(b). The reducing atmosphere equilibration due to higher water contents leads to higher protons and hence higher conductivities in SOFC mode. Higher O₂ pressure leads to slight increase in conductivity in SOEC mode by 0.001 S/cm which may be due to two reasons: (a) higher hole concentrations in BZY at higher O₂ partial pressures lead to an enhancement of potential on the Ag-side due concentrations gradients generated. This is not possible in reducing environments due to lower hole concentrations; and (b) more oxygen causes enhanced oxide and hydroxyl formation on the Ag surface, which leads to higher transfer of protons from the air-electrode side to the electrolyte, at the TPB.

The proton conductivity remains relatively constant in reducing environment in SOFC mode with an increase in the partial pressure of O₂, as seen in Fig. 5(d). However, in SOEC mode, it increases from 0.012 S/cm at 0.02 atm to 0.015 at 0.2 atm, followed by a decrease at a very high O₂ pressure of 2 atm. A very high O₂ pressure increases the cathodic polarization due to excess oxide ions on the cathodic side. In oxidizing atmospheres, there is a small increase in proton conductivity (both SOFC and SOEC) with an increase in O₂ partial pressure which increases the holes, creating a concentration gradient enhancing the emf nullifying the increased cathodic polarization.

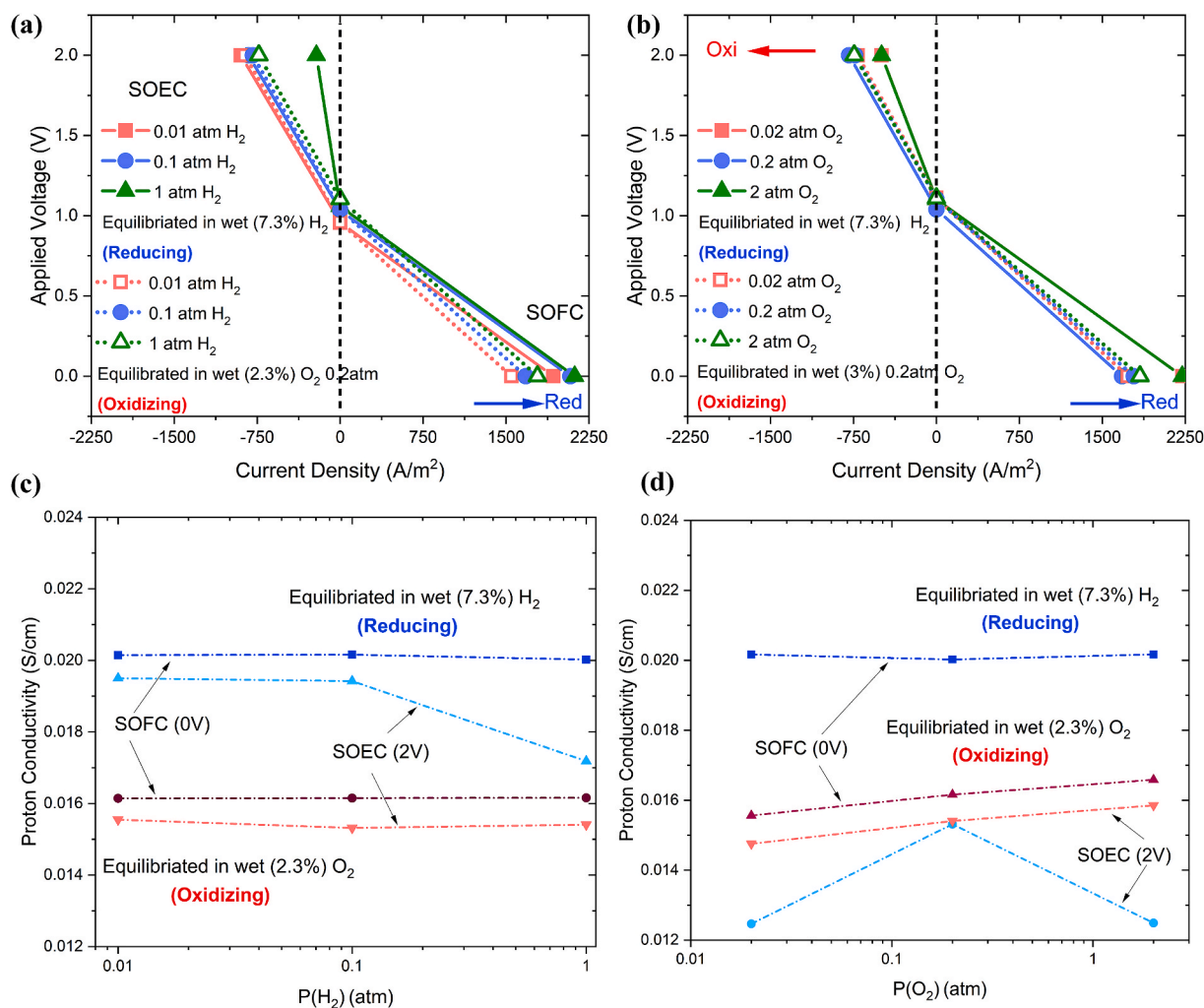


Fig. 5. The effect of (a) H₂ and (b) O₂ on the IV currents in SOFC and SOEC modes in oxidizing and reducing atmospheres. The effect of (c) H₂ and (d) O₂ on proton conductivity in the two modes under the different environments.

4.2. Effect of temperature and environment

The effect of both the temperature and the atmosphere the electrolyte is equilibrated in, on IV characteristics and proton conductivity can be seen in Fig. 6. As the temperature increases the current increases from 1416.2 A/m² 600 °C to 1724.9 A/m² at 700 °C in SOFC and from 367.7 A/m² 600 °C to 403.2 A/m² at 700 °C in SOEC mode. However, the increase of current in SOEC mode is not considerable as seen in Fig. 6(a), indicating the Pt/BZY/Ag SOC system is not an ideal one in SOEC mode. Better anode-electrolyte-cathode combinations for the SOFC mode have been reported recently. Having a Ni containing anode and PbBaCo₂O_{5+δ} as the cathode creates a current at 0 V of ~8000 A/m² at 600 °C with wet H₂ on the anodic side and ambient air on the cathodic side, as found by Bi et al. [94]. Even better performance was reported in a Ni-BZCY|BZY|SSC-SDC single cell of 2,750,000 A/m² at 0 V and 600 °C by Sun et al. [93] in wet H₂ atmosphere. The effect of various O₂ partial pressures and H₂O contents, the electrolyte is equilibrated in, keeping anodic (wet (7.3% H₂O) H₂) and cathodic (wet (3% H₂O) air) atmospheres the same, at a temperature of 600 °C, is shown in Fig. 6(b). The electrolyte equilibrated in highest H₂O (7.3%) content in SOFC and wet air in the SOEC mode seems to be leading to maximum proton current of 2120.6 A/m² and 735.9 A/m² in the respective modes. The simulations were repeated at 600 °C, 625 °C and 650 °C and the respective proton conductivities were calculated. The activation barrier for proton conductivity calculated from the Arrhenius relationship of conductivity with temperature appears to be highest (0.35 eV) when the electrolyte is equilibrated in a very oxidizing atmosphere (2 atm, 0.023 atm H₂O)

followed closely by a neutral environment with 0.01 atm O₂ (0.023 atm H₂O). The activation barrier is minimum at 0.294 eV for the case with the electrolyte equilibrated in reducing environment (0.073 atm H₂O) which might be ideal for low-temperature applications in SOFC mode. It should be noted that the concentrations of charge carriers are different in the three environments which is achieved by solving for Eqns (10-13). The concentration of charge carriers in the three environments are listed in Table 5

4.3. Design for new proton conductors

The performance of the SOCs depends on several factors some of which also happen to be the input parameters for the continuum model. A detailed analysis of the sensitivity of the input on the electrochemical characteristics is, therefore, necessary to isolate the critical factors affecting electrochemical characteristics and consequently, the performance of the SOC. The continuum model is found to depend on 36

Table 5
Concentration of charge carriers in different environments.

Concentration (M/m ³)	Reducing	Neutral	Oxidizing
Protons (H ⁺)	1401	1169	1554
Vacancies (V ⁻)	250	573	18
Holes (h ⁻)	1366	952	1678

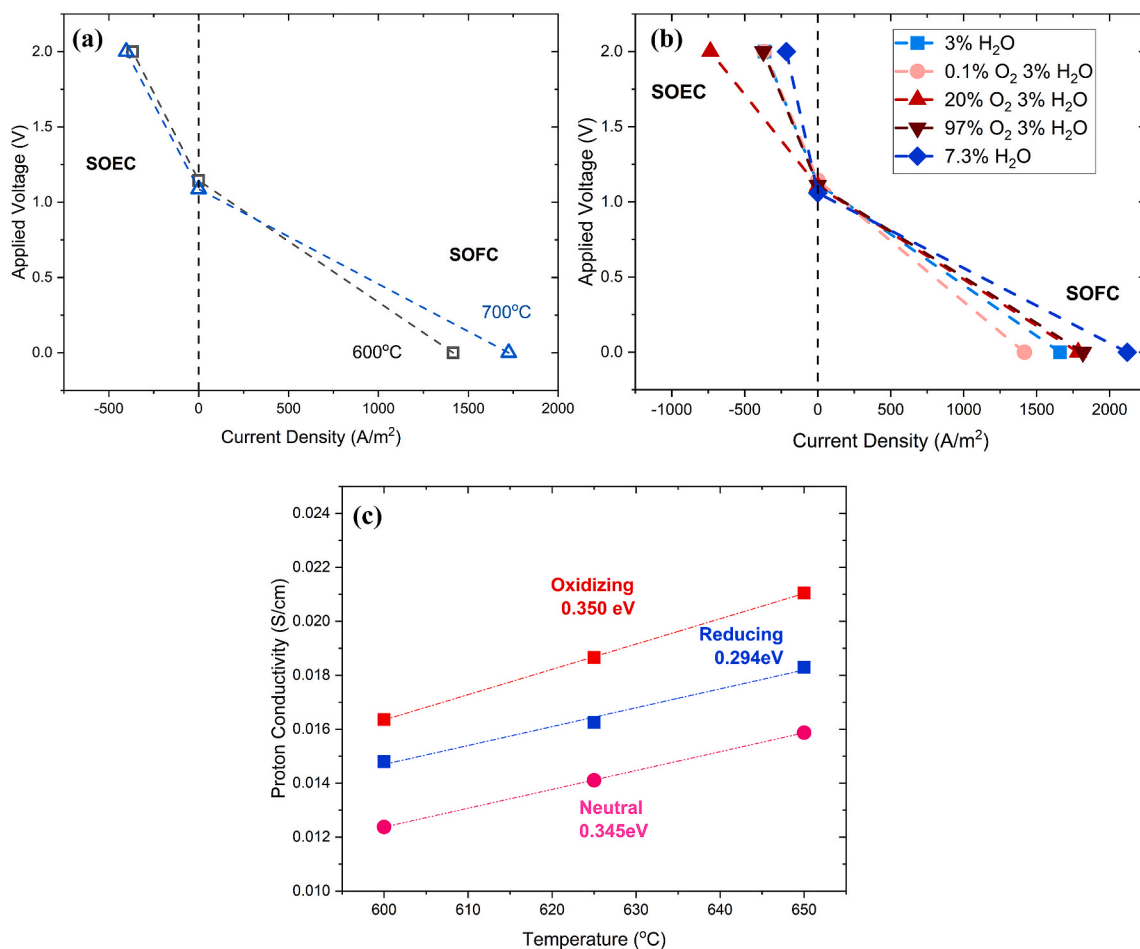


Fig. 6. a) IV characteristics under a neutral atmosphere at different IV temperatures; Effect of environments in which the BZY is equilibrated on (b) IV characteristics (c) activation energy for proton conductivity in SOFC mode.

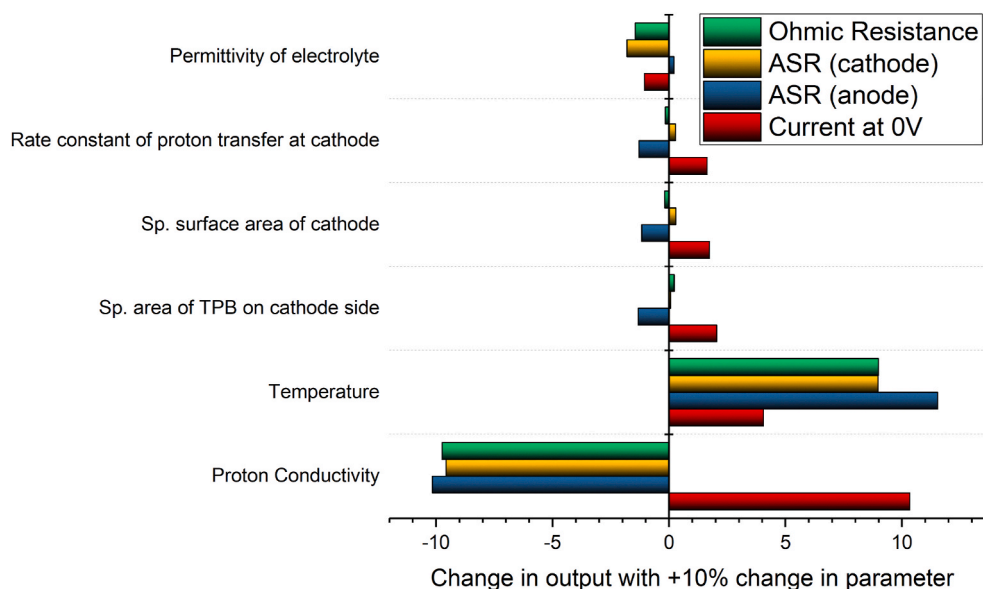


Fig. 7. Sensitivity of the electrochemical characteristics on the input parameters.

different parameters which are temperature, diffusion coefficients of the charged species, electrical properties of the electrolyte and the electrodes and the different rate constants of the reactions in the proposed reaction pathway. A detailed description of the parameters and a description of the model used for prediction of sensitivity are provided in the [Supplementary Material Section 5](#).

The important electrochemical parameters that determine performance are Current at 0 V (SOFC), Current at 2 V (SOEC), OCV, electrolytic, cathodic and anodic resistances. A detailed uncertainty quantification was performed for the influence of the 36 input parameters on these six output targets using Neural Networks as a surrogate model. The neural networks surrogate model was trained using the 1000 test case runs using random inputs following a gaussian distribution about the mean of the 36 individual input parameters. This surrogate model was then used to determine the sensitivity of the parameters on the above electrochemical target parameters.

Fig. 7 shows the sensitivity of the top 6 input parameters on the current at 0 V, cathodic, anodic polarization and Ohmic resistance, using the Neural Network surrogate model. The most critical parameters affecting performance are proton diffusivity, temperature, microstructural features at the cathode, rate constants for proton transfer at the TPB at BZY/cathode interfaces and permittivity of the electrolyte, in the decreasing order of importance. It should be noted that an increase of 0.02–0.09 eV in any of the energy barriers (Shown in [Supplementary Information Section 4](#)) causes a change of 23–69% in rate constant. From the sensitivity analysis, it is seen that such discrepancies in rate constants is within a maximum 4–14% error of the SOC characteristics. The error in underestimation of reaction barriers at the reactions at the TPBs which are calculated in this work using PBE are less than 10% of PBE + U. Also, PBE has been used for other DFT reaction barrier data adopted from literature. Therefore, we use PBE for the electrochemical characteristic estimation for sake of consistency. The effects of the parameters are mostly intuitive except for microstructure of the cathode and permittivity of the electrolyte.

Higher specific area of the surface and the TPB interface length leads to little change in cathodic resistance/polarization and Ohmic resistance but greatly enhances the current density by reducing the anodic polarization due to fast transport of protons into the electrolyte and consequently to the cathode. The specific surface area and TPB length can be increased by having smaller grains in the porous Ag cathodes.

While an increase in permittivity decreases the cathodic and ohmic resistances, which is advantageous for SOC performance, it also

decreases the current by increasing the anodic resistance. This effect can be understood based on two opposing effects of increasing the permittivity. On the one hand, increasing the permittivity leads to lower electrostatic energy of the charge carriers meaning, the electrolyte can accommodate larger concentrations of protons. Compared to an electrolyte with lower permittivity, a higher proton concentration is beneficial for proton conductivity. On the other hand, a higher permittivity leads to reduced electrostatic forces on the charged carriers making their transport difficult which is deleterious to the amount of proton current. Therefore, an intermediate, rather than a high or low permittivity of electrolytes in SOCs can lead to higher performances. This effect can be a recipe for design and experimentation of new proton-conducting electrolytes.

5. Conclusion

A multiscale model has been developed which could predict the electrochemical characteristics of IV in BZY based SOCs. The model has been validated against experimental observations. An approximate reaction pathway has been proposed for transfer of protons from the anode, across the electrolyte to the cathode. Density Functional Theory has been used to calculate the energy barriers for various reactions at the free surface of the electrodes and the TPBs of Pt/BZY/air and Ag/BZY/air. These barriers are used to calculate the rate constants for different reactions and diffusivities for various charged species. These parameters, along with accurate electrical and microstructural properties, are used in the continuum model to solve for the transport of the charged species in time.

Environment affects the type of charge carriers, while temperature affects transport. Both these have a considerable effect on reaction rates and hence the electrochemical characteristics. While the reducing H₂ containing environments have higher current densities for fuel cell mode operation, the oxidizing O₂ containing environments are suitable for electrolyzer cell mode operations. The activation energy of proton conductivity in oxidizing and neutral environments is higher making them less amenable for low-temperature operation than the reducing environments.

The proton diffusivity, temperature, microstructural features at the cathode, rate constants for proton transfer at the TPB at BZY/cathode interfaces and permittivity of the electrolyte, in the decreasing order of importance, are the most critical parameters affecting electrochemical performance of proton-conducting electrolyte based SOCs. The

permittivity of the electrolyte is crucial as it affects the concentration as well as the transport of protons. Mixing high permittivity solid oxides with low permittivity solid oxides can be a recipe for design and experimentation of new proton conductors.

CRedit authorship contribution statement

Pikee Priya: Methodology, Writing - original draft, Formal analysis.
N.R. Aluru: Funding acquisition, Supervision, Writing - review & editing.

Declaration of competing interest

No conflict of interest exists.

Acknowledgement

This work was supported by the National Science Foundation (USA) under grant # 1545907. This research is part of the Blue Waters sustained-petascale computing project, which is supported by the National Science Foundation (awards OCI-0725070 and ACI-1238993) and the state of Illinois. The authors acknowledge the use of the parallel computing resources Blue Waters provided by the National Center for Supercomputing Applications. Assistance from Linjian Ma who initiated the work, Chi Zhang who helped in data collection and Prof. Yuhang Jing for discussions on DFT methodology is gratefully acknowledged.

Appendix A. Supplementary data

Supplementary data to this article can be found online at <https://doi.org/10.1016/j.jpowsour.2020.228969>.

References

- [1] J. Hou, F. Liu, Z. Gong, Y. Wu, W. Liu, Different ceria-based materials Gd_{0.1}Ce_{0.9}O_{2-δ} and Sm_{0.075}Nd_{0.075}Ce_{0.85}O_{2-δ} for ceria-bismuth bilayer electrolyte high performance low temperature solid oxide fuel cells, *J. Power Sources* 299 (2015) 32–39, <https://doi.org/10.1016/j.jpowsour.2015.08.077>.
- [2] J. Hou, L. Bi, J. Qian, Z. Gong, Z. Zhu, W. Liu, A novel composite cathode Er_{0.4}Bi_{1.6}O₃-Pr_{0.5}Ba_{0.5}MnO_{3-δ} for ceria-bismuth bilayer electrolyte high performance low temperature solid oxide fuel cells, *J. Power Sources* 301 (2016) 306–311, <https://doi.org/10.1016/j.jpowsour.2015.10.018>.
- [3] M. Li, M. Zhao, F. Li, W. Zhou, V.K. Peterson, X. Xu, Z. Shao, I. Gentile, Z. Zhu, A niobium and tantalum co-doped perovskite cathode for solid oxide fuel cells operating below 500 °C, *Nat. Commun.* 8 (2017) 1–9, <https://doi.org/10.1038/ncomms13990>.
- [4] C. Duan, D. Hook, Y. Chen, J. Tong, R. O'Hayre, Zr and Y co-doped perovskite as a stable, high performance cathode for solid oxide fuel cells operating below 500°C, *Energy Environ. Sci.* 10 (2017) 176–182, <https://doi.org/10.1039/c6ee01915c>.
- [5] J. Di, M. Chen, C. Wang, J. Zheng, L. Fan, B. Zhu, Samarium doped ceria-(Li/Na) 2CO₃ composite electrolyte and its electrochemical properties in low temperature solid oxide fuel cell, *J. Power Sources* 195 (2010) 4695–4699, <https://doi.org/10.1016/j.jpowsour.2010.02.066>.
- [6] S. Ricote, A. Almansoori, M. Sanders, J. Tong, C. Duan, S. Nikodemski, R. O'Hayre, M. Shang, Readily processed protonic ceramic fuel cells with high performance at low temperatures (80–), *Science* 349 (2015) 1321–1326, <https://doi.org/10.1126/science.aab3987>.
- [7] Y. Zhu, W. Zhou, R. Ran, Y. Chen, Z. Shao, M. Liu, Promotion of oxygen reduction by exsolved silver nanoparticles on a perovskite scaffold for low-temperature solid oxide fuel cells, *Nano Lett.* 16 (2016) 512–518, <https://doi.org/10.1021/acs.nanolett.5b04160>.
- [8] L. Fan, P.C. Su, Layer-structured LiNi_{0.8}Co_{0.2}O₂: a new triple (H⁺/O₂-/e⁻) conducting cathode for low temperature proton conducting solid oxide fuel cells, *J. Power Sources* 306 (2016) 369–377, <https://doi.org/10.1016/j.jpowsour.2015.12.015>.
- [9] K.T. Lee, D.W. Jung, M.A. Camaratta, H.S. Yoon, J.S. Ahn, E.D. Wachsman, Gd_{0.1}Ce_{0.9}O₂-1.95/Er_{0.4}Bi_{1.6}O₃ bilayered electrolytes fabricated by a simple colloidal route using nano-sized Er_{0.4}Bi_{1.6}O₃ powders for high performance low temperature solid oxide fuel cells, *J. Power Sources* 205 (2012) 122–128, <https://doi.org/10.1016/j.jpowsour.2012.01.040>.
- [10] A. Evans, J. Martynczuk, D. Stender, C.W. Schneider, T. Lippert, M. Prestat, Low-temperature micro-solid oxide fuel cells with partially amorphous La_{0.6}Sr_{0.4}CoO_{3-δ} cathodes, *Adv. Energy Mater.* 5 (2015) 1–9, <https://doi.org/10.1002/aenm.201400747>.
- [11] S. Longo, M. Cellura, F. Guarino, M. Ferraro, V. Antonucci, G. Squadrito, Life Cycle Assessment of Solid Oxide Fuel Cells and Polymer Electrolyte Membrane Fuel Cells: A Review, Elsevier Ltd, 2017, <https://doi.org/10.1016/B978-0-12-811132-1.00006-7>.
- [12] A. Dubois, S. Ricote, R.J. Braun, Benchmarking the expected stack manufacturing cost of next generation, intermediate-temperature protonic ceramic fuel cells with solid oxide fuel cell technology, *J. Power Sources* 369 (2017) 65–77, <https://doi.org/10.1016/j.jpowsour.2017.09.024>.
- [13] H. Falk-Windisch, J.E. Svensson, J. Froitzheim, The effect of temperature on chromium vaporization and oxide scale growth on interconnect steels for Solid Oxide Fuel Cells, *J. Power Sources* 287 (2015) 25–35, <https://doi.org/10.1016/j.jpowsour.2015.04.040>.
- [14] J.T.S. Irvine, D. Neagu, M.C. Verbraeken, C. Chatzichristodoulou, C. Graves, M. B. Mogensen, Evolution of the electrochemical interface in high-temperature fuel cells and electrolyzers, *Nat. Energy.* 1 (2016) 1–13, <https://doi.org/10.1038/energy.2015.14>.
- [15] D. The, S. Grieshammer, M. Schroeder, M. Martin, M. Al Daroukh, F. Tietz, J. Scheffold, A. Brisse, Microstructural comparison of solid oxide electrolyser cells operated for 6100 h and 9000 h, *J. Power Sources* 275 (2015) 901–911, <https://doi.org/10.1016/j.jpowsour.2014.10.188>.
- [16] S.H. Jensen, C. Graves, M. Mogensen, C. Wendel, R. Braun, G. Hughes, Z. Gao, S. A. Barnett, Large-scale electricity storage utilizing reversible solid oxide cells combined with underground storage of CO₂ and CH₄, *Energy Environ. Sci.* 8 (2015) 2471–2479, <https://doi.org/10.1039/c5ee01485a>.
- [17] L. Yan, X. Rui, G. Chen, W. Xu, G. Zou, H. Luo, Recent advances in nanostructured Nb-based oxides for electrochemical energy storage, *Nanoscale* 8 (2016) 8443–8465, <https://doi.org/10.1039/c6nr01340f>.
- [18] B. Molero-Sánchez, J. Prado-Gonjal, D. Ávila-Brandé, M. Chen, E. Morán, V. Birss, High performance La_{0.3}Ca_{0.7}Cr_{0.3}Fe_{0.7}O_{3-δ} air electrode for reversible solid oxide fuel cell applications, *Int. J. Hydrogen Energy* 40 (2015) 1902–1910, <https://doi.org/10.1016/j.ijhydene.2014.11.127>.
- [19] S.Y. Gómez, D. Hotza, Current developments in reversible solid oxide fuel cells, *Renew. Sustain. Energy Rev.* 61 (2016) 155–174, <https://doi.org/10.1016/j.rser.2016.03.005>.
- [20] C. Graves, S.D. Ebbesen, S.H. Jensen, S.B. Simonsen, M.B. Mogensen, Eliminating degradation in solid oxide electrochemical cells by reversible operation, *Nat. Mater.* 14 (2015) 239–244, <https://doi.org/10.1038/nmat4165>.
- [21] K. Chen, S.S. Liu, N. Ai, M. Koyama, S.P. Jiang, Why solid oxide cells can be reversibly operated in solid oxide electrolysis cell and fuel cell modes? *Phys. Chem. Chem. Phys.* 17 (2015) 31308–31315, <https://doi.org/10.1039/c5cp05065k>.
- [22] S. Yang, Y. Wen, S. Zhang, S. Gu, Z. Wen, X. Ye, Performance and stability of BaCe_{0.8-x}Zr_{0.2}In_xO_{3-δ}-Δ-based materials and reversible solid oxide cells working at intermediate temperature, *Int. J. Hydrogen Energy* 42 (2017) 28549–28558, <https://doi.org/10.1016/j.ijhydene.2017.09.159>.
- [23] J. Lyagaeva, N. Danilov, G. Vdovin, J. Bu, D. Medvedev, A. Demin, P. Tsiakaras, A new Dy-doped BaCeO₃-BaZrO₃ proton-conducting material as a promising electrolyte for reversible solid oxide fuel cells, *J. Mater. Chem. A.* 4 (2016) 15390–15399, <https://doi.org/10.1039/c6ta06414k>.
- [24] L. Bi, S. Boulfrad, E. Traversa, Reversible solid oxide fuel cells (R-SOFCs) with chemically stable proton-conducting oxides, *Solid State Ionics* 275 (2015) 101–105, <https://doi.org/10.1016/j.ssi.2015.03.006>.
- [25] G. Chen, Y. Luo, W. Sun, H. Liu, Y. Ding, Y. Li, S. Geng, K. Yu, G. Liu, Electrochemical performance of a new structured low temperature SOFC with BZY electrolyte, *Int. J. Hydrogen Energy* 43 (2018) 12765–12772, <https://doi.org/10.1016/j.ijhydene.2018.04.006>.
- [26] D. Pergolesi, E. Fabbri, A. D'Epifanio, E. Di Bartolomeo, A. Tebano, S. Sanna, S. Licocchia, G. Balestrino, E. Traversa, High proton conduction in grain-boundary-free yttrium-doped barium zirconate films grown by pulsed laser deposition, *Nat. Mater.* 9 (2010) 846–852, <https://doi.org/10.1038/nmat2837>.
- [27] S.B.C. Duval, P. Holtappels, U.F. Vogt, E. Pomjakushina, K. Conder, U. Stimming, T. Graule, Electrical conductivity of the proton conductor BaZr_{0.9}Y_{0.1}O_{3-δ} obtained by high temperature annealing, *Solid State Ionics* 178 (2007) 1437–1441, <https://doi.org/10.1016/j.ssi.2007.08.006>.
- [28] G. Kresse, J. Furthmüller, Efficiency of ab-initio total energy calculations for metals and semiconductors using a plane-wave basis set, *Comput. Mater. Sci.* 6 (1996) 15–50, [https://doi.org/10.1016/0927-0256\(96\)00008-0](https://doi.org/10.1016/0927-0256(96)00008-0).
- [29] G. Kresse, J. Furthmüller, Efficient iterative schemes for ab initio total-energy calculations using a plane-wave basis set, *Phys. Rev. B* 54 (1996) 11169–11186, <https://doi.org/10.1103/PhysRevB.54.11169>.
- [30] G. Kresse, J. Hafner, Ab initio molecular dynamics for open-shell transition metals, *Phys. Rev. B* 48 (1993) 13115–13118, <https://doi.org/10.1103/PhysRevB.48.13115>.
- [31] K.J. Laidler, M.C. King, The development of transition-state theory, *J. Phys. Chem.* 87 (1983) 2657–2664, <https://doi.org/10.1021/j100238a002>.
- [32] K.P. Recknagle, R.E. Williford, L.A. Chick, D.R. Rector, M.A. Khaleel, Three-dimensional thermo-fluid electrochemical modeling of planar SOFC stacks, *J. Power Sources* 113 (2003) 109–114, [https://doi.org/10.1016/S0378-7753\(02\)00487-1](https://doi.org/10.1016/S0378-7753(02)00487-1).
- [33] R. Ferguson, M. Fiard, R. Herbin, Three-dimensional numerical simulation for various geometries of solid oxide fuel cells, *J. Power Sources* 58 (1996) 109–122, [https://doi.org/10.1016/0378-7753\(95\)02269-4](https://doi.org/10.1016/0378-7753(95)02269-4).
- [34] H. Yakabe, T. Ogiwara, M. Hishinuma, I. Yasuda, 3-D model calculation for planar SOFC, *J. Power Sources* 102 (2001) 144–154, [https://doi.org/10.1016/S0378-7753\(01\)00792-3](https://doi.org/10.1016/S0378-7753(01)00792-3).
- [35] P. Costamagna, A. Selimovic, M. Del Borghi, G. Agnew, Electrochemical model of the integrated planar solid oxide fuel cell (IP-SOFC), *Chem. Eng. J.* 102 (2004) 61–69, <https://doi.org/10.1016/j.cej.2004.02.005>.

- [36] P. Aguiar, C.S. Adjiman, N.P. Brandon, Anode-supported intermediate temperature direct internal reforming solid oxide fuel cell. I: model-based steady-state performance, *J. Power Sources* 138 (2004) 120–136, <https://doi.org/10.1016/j.jpowsour.2004.06.040>.
- [37] U. Pasaogullari, C.-Y. Wang, Computational fluid dynamics modeling of solid oxide fuel cells, *ECS Proc* 7 (2003) 1403–1412, <https://doi.org/10.1149/200307.1403pv>.
- [38] M.A. Khaleel, Z. Lin, P. Singh, W. Surdoyal, D. Collin, A finite element analysis modeling tool for solid oxide fuel cell development: coupled electrochemistry, thermal and flow analysis in MARC®, *J. Power Sources* 130 (2004) 136–148, <https://doi.org/10.1016/j.jpowsour.2003.11.074>.
- [39] V.M. Janardhanan, O. Deutschmann, CFD analysis of a solid oxide fuel cell with internal reforming: coupled interactions of transport, heterogeneous catalysis and electrochemical processes, *J. Power Sources* 162 (2006) 1192–1202, <https://doi.org/10.1016/j.jpowsour.2006.08.017>.
- [40] Q. Cai, C.S. Adjiman, N.P. Brandon, Modelling the 3D microstructure and performance of solid oxide fuel cell electrodes: computational parameters, *Electrochim. Acta* 56 (2011) 5804–5814, <https://doi.org/10.1016/j.electacta.2011.04.065>.
- [41] W.Y. Lee, D. Wee, A.F. Ghoniem, An improved one-dimensional membrane-electrode assembly model to predict the performance of solid oxide fuel cell including the limiting current density, *J. Power Sources* 186 (2009) 417–427, <https://doi.org/10.1016/j.jpowsour.2008.10.009>.
- [42] J.H. Nam, D.H. Jeon, A comprehensive micro-scale model for transport and reaction in intermediate temperature solid oxide fuel cells, *Electrochim. Acta* 51 (2006) 3446–3460, <https://doi.org/10.1016/j.electacta.2005.09.041>.
- [43] A.S. Martinez, J. Brouwer, Percolation modeling investigation of TPB formation in a solid oxide fuel cell electrode-electrolyte interface, *Electrochim. Acta* 53 (2008) 3597–3609, <https://doi.org/10.1016/j.electacta.2007.11.082>.
- [44] D. Gostovic, J.R. Smith, D.P. Kundinger, K.S. Jones, E.D. Wachsman, Three-Dimensional reconstruction of porous LSCF cathodes, *Electrochem. Solid State Lett.* 10 (2007) B214, <https://doi.org/10.1149/1.2794672>.
- [45] J. Joos, T. Carraro, A. Weber, E. Ivers-Tiffée, Reconstruction of porous electrodes by FIB/SEM for detailed microstructure modeling, *J. Power Sources* 196 (2011) 7302–7307, <https://doi.org/10.1016/j.jpowsour.2010.10.006>.
- [46] M.E. Lynch, D. Ding, W.M. Harris, J.J. Lombardo, G.J. Nelson, W.K.S. Chiu, M. Liu, Flexible multiphysics simulation of porous electrodes: conformal to 3D reconstructed microstructures, *Nanomater. Energy* 2 (2013) 105–115, <https://doi.org/10.1016/j.nanoen.2012.08.002>.
- [47] G. Kresse, J. Hafner, Ab initio molecular dynamics for liquid metals, *Phys. Rev. B* 47 (1993) 558–561, <https://doi.org/10.1103/PhysRevB.47.558>.
- [48] J.P. Perdew, K. Burke, M. Ernzerhof, Generalized gradient approximation made simple, *Phys. Rev. Lett.* 77 (1996) 3865–3868, <https://doi.org/10.1103/PhysRevLett.77.3865>.
- [49] H. Hellman, *Introduction to Quantum Chemistry*, 1937.
- [50] R.P. Feynman, Forces in molecules, *Phys. Rev.* 56 (1939) 340–343, <https://doi.org/10.1103/PhysRev.56.340>.
- [51] G. Kresse, D. Joubert, From ultrasoft pseudopotentials to the projector augmented-wave method, *Phys. Rev. B* 59 (1999) 1758–1775, <https://doi.org/10.1103/PhysRevB.59.1758>.
- [52] G. Mills, H. Jónsson, G.K. Schenter, Reversible work transition state theory: application to dissociative adsorption of hydrogen, *Surf. Sci.* 324 (1995) 305–337, [https://doi.org/10.1016/0039-6028\(94\)00731-4](https://doi.org/10.1016/0039-6028(94)00731-4).
- [53] G. Henkelman, B.P. Uberuaga, H. Jónsson, Climbing image nudged elastic band method for finding saddle points and minimum energy paths, *J. Chem. Phys.* 113 (2000) 9901–9904, <https://doi.org/10.1063/1.1329672>.
- [54] J.D. Pack, H.J. Monkhorst, Special points for Brillouin-zone integrations, *Phys. Rev. B* 16 (1977) 1748–1749, <https://doi.org/10.1103/PhysRevB.16.1748>.
- [55] T.T.T. Hanh, Y. Takimoto, O. Sugino, First-principles thermodynamic description of hydrogen electroadsorption on the Pt(111) surface, *Surf. Sci.* 625 (2014) 104–111, <https://doi.org/10.1016/j.susc.2014.03.006>.
- [56] I.A. Pašti, N.M. Gavrilov, S.V. Mentus, Hydrogen adsorption on palladium and platinum overlayers: DFT study, *Adv. Phys. Chem.* 2011 (2011), <https://doi.org/10.1155/2011/305634>.
- [57] K. Kodchakorn, V.S. Lee, J. Yana, P. Nimmanpipug, Density functional theory calculations of hydrogen dissociative adsorption on platinum-involved alloy surfaces, *Surf. Coating Technol.* 306 (2016) 35–40, <https://doi.org/10.1016/j.surfcoat.2016.04.014>.
- [58] B. Poelsema, K. Lenz, G. Comsa, The dissociative adsorption of hydrogen on defect-free Pt(111), *J. Phys. Condens. Matter* 22 (2010), <https://doi.org/10.1088/0953-8984/22/30/304006>.
- [59] N.B. Arboleda, H. Kasai, W.A. Diño, H. Nakanishi, Potential energy of H₂ dissociation and adsorption on Pt(111) surface: first-principles calculation, *Japanese J. Appl. Physics, Part 1 Regul. Pap. Short Notes Rev. Pap.* 46 (2007) 4233–4237, <https://doi.org/10.1143/JJAP.46.4233>.
- [60] I. Hamada, Y. Morikawa, Density-functional analysis of hydrogen on Pt(111): electric field, solvent, and coverage effects (Journal of Physical Chemistry C, 112C (10897)), *J. Phys. Chem. C* 112 (2008), 17486, <https://doi.org/10.1021/jp808509k>.
- [61] R.A. Olsen, G.J. Kroes, E.J. Baerends, Atomic and molecular hydrogen interacting with Pt(111), *J. Chem. Phys.* 111 (1999) 11155–11163, <https://doi.org/10.1063/1.480473>.
- [62] L.J. Richter, W. Ho, Vibrational spectroscopy of H on Pt(111): evidence for universally soft parallel modes, *Phys. Rev. B* 36 (1987) 9797–9800, <https://doi.org/10.1103/PhysRevB.36.9797>.
- [63] C. Zhou, J. Wu, A. Nie, R.C. Forrey, A. Tachibana, H. Cheng, On the sequential hydrogen dissociative chemisorption on small platinum clusters: a density functional theory study, *J. Phys. Chem. C* 111 (2007) 12773–12778, <https://doi.org/10.1021/jp073597e>.
- [64] T.S. Zyubina, A.S. Zyubin, Y.A. Dobrovolskii, V.M. Volokhov, A.V. Arsatov, Z. G. Bazhanova, Dissociative adsorption of molecular hydrogen onto Pt6 and Pt19 platinum clusters located on the tin dioxide surface: quantum-chemical modeling, *Russ. J. Inorg. Chem.* 56 (2011) 1579–1588, <https://doi.org/10.1134/S0036023611100287>.
- [65] L. Kristinsdóttir, E. Skúlason, A systematic DFT study of hydrogen diffusion on transition metal surfaces, *Surf. Sci.* 606 (2012) 1400–1404, <https://doi.org/10.1016/j.susc.2012.04.028>.
- [66] W. Dononelli, T. Klüner, CO adsorption and oxygen activation on group 11 nanoparticles—a combined DFT and high level CCSD(T) study about size effects and activation processes, *Faraday Discuss* 208 (2018) 105–121, <https://doi.org/10.1039/c7fd00225d>.
- [67] M. Yan, Z.Q. Huang, Y. Zhang, C.R. Chang, Trends in water-promoted oxygen dissociation on the transition metal surfaces from first principles, *Phys. Chem. Chem. Phys.* 19 (2017) 2364–2371, <https://doi.org/10.1039/c6cp06974f>.
- [68] W.X. Li, C. Stampfl, M. Scheffler, Oxygen adsorption on Ag(111): a density-functional theory investigation, *Phys. Rev. B Condens. Matter* 65 (2002) 1–19, <https://doi.org/10.1103/PhysRevB.65.075407>.
- [69] I. Goikoetxea, J. Beltrán, J. Meyer, J.I. Juaristi, M. Alducin, K. Reuter, Non-adiabatic effects during the dissociative adsorption of O₂ at Ag(111)? A first-principles divide and conquer study, *New J. Phys.* 14 (2012), <https://doi.org/10.1088/1367-2630/14/1/013050>.
- [70] H. Su, M. Yang, X. Bao, W. Li, *The Effect of Water on the CO Oxidation on Ag (111) and Au (111) Surfaces, A First-Principle Study*, 2008, pp. 17303–17310.
- [71] J.H. Wang, M.L. Liu, M.C. Lin, Oxygen reduction reactions in the SOFC cathode of Ag/CeO₂, *Solid State Ionics* 177 (2006) 939–947, <https://doi.org/10.1016/j.ssi.2006.02.029>.
- [72] A. Montoya, B.S. Haynes, Reactions of hydroxyl on the topmost layer of Ag(111): a density functional theory study, *J. Phys. Chem. C* 111 (2007) 1333–1341, <https://doi.org/10.1021/jp065576a>.
- [73] G.C. Wang, S.X. Tao, X.H. Bu, A systematic theoretical study of water dissociation on clean and oxygen-preadsorbed transition metals, *J. Catal.* 244 (2006) 10–16, <https://doi.org/10.1016/j.jcat.2006.07.034>.
- [74] A. Michaelides, Density functional theory simulations of water – metal interfaces: waltzing waters, a novel 2D ice phase, and more, *Appl. Phys. A* 85 (2006) 415–425, <https://doi.org/10.1007/s00339-006-3695-9>.
- [75] V.A. Ranea, A. Michaelides, R. Ramirez, J.A. Verge, P.L. De Andres, D.A. King, Density functional theory study of the interaction of monomeric water with the Ag {111} surface, *Phys. Rev. B* 69 (2004) 1–9, <https://doi.org/10.1103/PhysRevB.69.205411>.
- [76] L. Ma, P. Priya, N.R. Aluru, A multiscale model for electrochemical reactions in LSCF based solid oxide cells, *J. Electrochem. Soc.* 165 (2018) F1232–F1241, <https://doi.org/10.1149/2.0921814jes>.
- [77] R. Suwanwarangkul, E. Croiset, M.W. Fowler, P.L. Douglas, E. Entchev, M. A. Douglas, Performance comparison of Pick’s, dusty-gas and Stefan-Maxwell models to predict the concentration overpotential of a SOFC anode, *J. Power Sources* 122 (2003) 9–18, [https://doi.org/10.1016/S0378-7753\(02\)00724-3](https://doi.org/10.1016/S0378-7753(02)00724-3).
- [78] K.D. Kreuer, S. Adams, W. Münch, A. Fuchs, U. Klock, J. Maier, Proton conducting alkaline earth zirconates and titanates for high drain electrochemical applications, *Solid State Ionics* 145 (2001) 295–306, [https://doi.org/10.1016/S0167-2738\(01\)00953-5](https://doi.org/10.1016/S0167-2738(01)00953-5).
- [79] A.V. Kuz’min, V.B. Balakireva, S.V. Plaksin, V.P. Gorelov, Total and hole conductivity in the BaZr_{1-x}Y_xO₃ – α system ($x = 0.02$ – 0.20) in oxidizing atmosphere, *Russ. J. Electrochem.* 45 (2009) 1351–1357, <https://doi.org/10.1134/s1023193509120064>.
- [80] Y. Yamazaki, F. Blanc, Y. Okuyama, L. Buannic, J.C. Lucio-Vega, C.P. Grey, S. M. Haile, Proton trapping in yttrium-doped barium zirconate, *Nat. Mater.* 12 (2013) 647–651, <https://doi.org/10.1038/nmat3638>.
- [81] M. Shishkin, T. Ziegler, Oxidation of H₂, CH₄, and CO molecules at the interface between nickel and yttria-stabilized zirconia: a theoretical study based on DFT, *J. Phys. Chem. C* 113 (2009) 21667–21678, <https://doi.org/10.1021/jp905615c>.
- [82] M. Malagoli, M.L. Liu, H.C. Park, A. Bongiorno, Protons crossing triple phase boundaries based on a metal catalyst, Pd or Ni, and barium zirconate, *Phys. Chem. Chem. Phys.* 15 (2013) 12525–12529, <https://doi.org/10.1039/c3cp51863a>.
- [83] R.C. Robert, Molecular diffusion of gases, *AIP Handb.*, (n.d.) 249, <https://web.mit.edu/references-fall/aip>.
- [84] A. Montoya, B.S. Haynes, Reactions of hydroxyl on the topmost layer of Ag(111): a density functional theory study, *J. Phys. Chem. C* 111 (2007) 1333–1341, <https://doi.org/10.1021/jp065576a>.
- [85] P. Ptáček, F. Šoukal, T. Opravil, Introduction to the transition state theory. *Introd. Eff. Mass Act. Complex Discuss. Wave Funct. This Instant.*, InTech, 2018, p. 13, <https://doi.org/10.5772/intechopen.78705>.
- [86] H. Eyring, The activated complex in chemical reactions, *J. Chem. Phys.* 3 (1935) 107–115, <https://doi.org/10.1063/1.1749604>.
- [87] H.G. Weller, G. Tabor, H. Jasak, C. Fureby, A tensorial approach to computational continuum mechanics using object-oriented techniques, *Comput. Phys.* 12 (1998) 620, <https://doi.org/10.1063/1.168744>.
- [88] H. Jasak, A. Jemcov, Z. Tukovic, OpenFOAM: a C++ library for complex physics simulations, *Int. Work. Coupled Methods Numer. Dyn. m* (2007) 1–20.
- [89] F. Iguchi, M. Nagai, N. Sata, H. Yugami, Fabrication and generation of intermediate temperature operating SOFC based on Y-doped BaZrO₃ Proton conducting oxides, *ECS Trans* 25 (2009) 1759–1766.

- [90] J.E. Hillard, L. Lawson, *Stereology and Stochastic Geometry*, Springer Science and Business Media, 2003.
- [91] K.D. Kreuer, Proton-conducting oxides, *Annu. Rev. Mater. Res.* 33 (2003) 333–359, <https://doi.org/10.1146/annurev.matsci.33.022802.091825>.
- [92] D.S. Tsvetkov, I.L. Ivanov, D.A. Malyskin, V.V. Sereda, A. Yu Zuev, Red-ox energetics and holes trapping in yttrium-substituted barium zirconate BaZr_{0.9}Y_{0.1}O_{2.95}, *J. Electrochem. Soc.* 166 (2019) F232–F238, <https://doi.org/10.1149/2.0481904jes>.
- [93] W. Sun, L. Yan, Z. Shi, Z. Zhu, W. Liu, Fabrication and performance of a proton-conducting solid oxide fuel cell based on a thin BaZr_{0.8}Y_{0.2}O_{3-δ} electrolyte membrane, *J. Power Sources* 195 (2010) 4727–4730, <https://doi.org/10.1016/j.jpowsour.2010.02.012>.
- [94] L. Bi, E.H. Da'as, S.P. Shafi, Proton-conducting solid oxide fuel cell (SOFC) with Y-doped BaZrO₃ electrolyte, *Electrochem. Commun.* 80 (2017) 20–23, <https://doi.org/10.1016/j.elecom.2017.05.006>.